communications physics

ARTICLE

https://doi.org/10.1038/s42005-021-00718-w OPEN

# Particle-hole asymmetry in the dynamical spin and charge responses of corner-shared 1D cuprates

Shaozhi Li [1✉], Alberto Nocera[2,3], Umesh Kumar [4] & Steven Johnston[5,6✉]

Although many experiments imply that oxygen orbitals play an essential role in the high-temperature superconducting cuprates, their precise role in collective spin and charge excitations and superconductivity is not yet fully understood. Here, we study the doping-dependent dynamical spin and charge structure factors of single and multi-orbital (*pd*) models for doped one-dimensional corner-shared spin-chain cuprates using several numerically exact methods. In doing so, we determine the orbital composition of the collective spin and charge excitations of cuprates, with important implications for our understanding of these materials. For example, we observe a particle-hole asymmetry in the orbital-resolved charge excitations, which is directly relevant to resonant inelastic x-ray scattering experiments and not captured by the single-band Hubbard model. Our results imply that one must explicitly include the oxygen degrees of freedom in order to fully understand some experimental observations on cuprate materials.

[1] Materials Science and Technology Division, Oak Ridge National Laboratory, Oak Ridge, TN, USA. [2] Stewart Blusson Quantum Matter Institute, University of British Columbia, Vancouver, BC, Canada. [3] Department of Physics Astronomy, University of British Columbia, Vancouver, BC, Canada. [4] Theoretical Division, T-4, Los Alamos National Laboratory, Los Alamos, NM, USA. [5] Department of Physics and Astronomy, The University of Tennessee, Knoxville, TN, USA. [6] Joint Institute of Advanced Materials at The University of Tennessee, Knoxville, TN, USA. ✉email: lis1@ornl.gov; sjohn145@utk.edu

The high-temperature (high-$T_c$) superconducting cuprates are governed by multiple intertwined orders, including unconventional superconductivity, pseudogap behavior, and various spin- and charge-orders[1]. Determining how well the single-band Hubbard model describes these orders and their associated dynamical fluctuations has become a frontier problem in condensed matter physics[2–4]. Nevertheless, significant progress has been made towards understanding the physics of the single-band Hubbard model, including its superconducting[3–7] and normal-state transport properties[8–10], its pseudogap[11–13], and stripe orders[14–17], and its dynamical response functions[11,18–20]. While it is now clear that the predictions of the single-band Hubbard model are consistent with many experimental observations in the cuprates, recent x-ray scattering and nuclear magnetic resonance experiments have implied that the oxygen $2p$ orbitals provide important contributions to the spin- and charge-orders[21–23]. These observations raise questions on the validity of the single-band Hubbard model for describing some properties of the cuprates, including the fluctuations of their intertwined orders.

Studying the ground and excited-state properties of the single- and multi-band Hubbard model on large two-dimensional (2D) lattices is challenging. For example, theoretical studies using dynamical mean-field theory and its cluster and diagrammatic extensions[24–27] have been limited to relatively small clusters. The study of the Hubbard model can be extended to larger lattices with determinant quantum Monte Carlo (DQMC)[9,17,18,28,29] but this method is more limited by the sign problem in comparison to embedded cluster methods. Some zero temperature techniques, such as the tensor network[30,31] and the path-constrained auxiliary-field quantum Monte Carlo[32] can access large lattices but have difficulty in calculating the single- and two-particle dynamical response functions probed by angle-resolved photoemission (ARPES), inelastic neutron scattering (INS), and resonant inelastic x-ray scattering (RIXS) experiments. Importantly, contrasting results obtained from the single-band model with multi-orbital models adds another layer of difficulty since the inclusion of the O $2p$ orbitals significantly increases the complexity of the problem[29,33–35].

In this work, we study single- and multi-orbital models for quasi-one-dimensional (1D) corner-shared spin-chain cuprates like $Sr_2CuO_3$ and the recently synthesized doped chains $Ba_{2-x}Sr_xCuO_{3+\delta}$[36,37]. Specifically, we compute and contrast the momentum-resolved dynamical spin and charge responses in these models using DQMC, density matrix renormalization group (DMRG), and exact diagonalization (ED, see Supplementary Note 1). By focusing on 1D cuprate models, we can perform reliable calculations for the single- and two-particle response functions for large system sizes with good momentum resolution, even in the multi-orbital case. These calculations are enabled by the fact that 1D systems generally have manageable fermion sign problems[38] and algorithmic advances in computing dynamical response functions using DMRG[39,40].

## Results

**Model for the corner-shared spin chains**. The active orbitals in spin-chain cuprates like $Sr_2CuO_3$ and $Ba_{2-x}Sr_xCuO_{3+\delta}$ are located in their $CuO_4$ plaquettes, which are arranged in a corner-shared geometry, as shown in Fig. 1a. $Sr_2CuO_3$ has been extensively studied both experimentally[41–46] and using single-band models like the Heisenberg model, the $t-J$ model[41–44,46,47], and the extended Hubbard model[48,49]. These models generally provide an excellent description of the magnetic excitations—in this case, a multi-spinon continuum—observed in INS[41–44] and RIXS[45,46] experiments. The spin and charge excitations of doped samples have received comparatively less attention because doping electrons or holes in $Sr_2CuO_3$ has proved to be challenging[50–52]. However, the $Ba_{2-x}Sr_xCuO_{3+\delta}$ system offers new possibilities in this regard[36,37].

We consider a four-orbital $pd$-model for corner-shared cuprates, which includes the Cu $3d_{x^2-y^2}$ and O $2p_{x/y}$ orbitals near the Fermi level, (Fig. 1a). The Hamiltonian for the four-orbital $pd$-model, written in hole language, is given by

$$\begin{aligned} H = &(\epsilon_d - \mu)\sum_{i,\sigma}\hat{n}^d_{i,\sigma} + \sum_{j,\gamma,\sigma}(\epsilon_{p,\gamma}-\mu)\hat{n}^p_{j,\gamma,\sigma} \\ &+ \sum_{\langle i,j\rangle\gamma,\sigma} t^{ij}_{pd}\left(d^\dagger_{i,\sigma}p_{j,\gamma,\sigma} + h.c.\right) + \sum_{\substack{\langle j,j'\rangle \\ \gamma,\gamma',\sigma}} t^{jj'}_{pp}p^\dagger_{j,\gamma,\sigma}p_{j',\gamma',\sigma} \\ &+ U_d\sum_i \hat{n}^d_{i,\uparrow}\hat{n}^d_{i,\downarrow} + U_p\sum_{j,\gamma}\hat{n}^p_{j,\gamma,\uparrow}\hat{n}^p_{j,\gamma,\downarrow} + U_{pd}\sum_{\substack{\langle i,j,\gamma\rangle \\ \sigma,\sigma'}}\hat{n}^d_{i,\sigma}\hat{n}^p_{j,\gamma,\sigma'}. \end{aligned} \tag{1}$$

Here, $\langle\cdots\rangle$ denotes a sum over nearest neighbor orbitals; $d^\dagger_{i,\sigma}$ and $p^\dagger_{j,\gamma,\sigma}$ create a hole with spin $\sigma$ ($=\uparrow,\downarrow$) on the $i$th Cu $3d_{x^2-y^2}$ orbital and the $j$th O $2p_\gamma$ ($\gamma = x, \pm y$) orbital, respectively; $\epsilon_d$ and $\epsilon_{p,\gamma}$ are the onsite energies; $\hat{n}^d_{i,\sigma}$ and $\hat{n}^p_{j,\gamma,\sigma}$ are the number operators for the Cu $3d_{x^2-y^2}$ orbital and O $2p_\gamma$ orbital, respectively; $t^{ij}_{pd}$ and $t^{jj'}_{pp}$ are the nearest-neighbor Cu−O and O−O hopping integrals, whose phase factors are drawn in Fig. 1a; $U_d$ and $U_p$ are the onsite Hubbard interactions on the Cu and O orbitals, respectively, and $U_{pd}$ is the nearest-neighbor Cu−O Coulomb repulsion; Finally, $\mu$ is the chemical potential, which is adjusted to control the hole density in our DQMC simulations. Throughout, we adopt parameters determined from density functional theory calculations and comparisons to experiments[53,54]. Specifically, we set (in units of eV) $\epsilon_d = 0$, $\epsilon_{p,x} = 3$, $\epsilon_{p,y} = 3.5$, $|t_{(p,x)d}| = 1.5$, $|t_{(p,y)d}| = 1.8$, $|t_{pp}| = 0.75$, $U_d = 8$, $U_p = 4$, and $U_{pd} = 1$. For these parameters, 60% of the holes are distributed on the Cu orbitals and 40% of the holes reside on the O orbitals at half filling (see Supplementary Note 2).

To isolate the influence of the oxygen degrees of freedom and assess the validity of a single-band effective model, we also studied a single-band $t$-$t'$ Hubbard model with model parameters selected to reproduce results from our multi-orbital model (see Supplementary Note 3). To remain consistent with the $pd$-model, our single-band Hubbard model is also written in the hole language, and is given by

$$H = -\mu\sum_{i,\sigma}\hat{n}_{i,\sigma} + \sum_{i,\sigma}t_{i,j}c^\dagger_{i,\sigma}c_{j,\sigma} + U\sum_i \hat{n}_{i,\uparrow}\hat{n}_{i,\downarrow}. \tag{2}$$

Here, $t_{i,j} = t$ and $t'$ are the nearest- and next-nearest-neighbor hopping integrals (we set all longer range hopping to zero). We adopt $t = 0.5$ eV based on the analysis in ref. 55. To determine the remaining parameters, we adjusted $t'$ and $U$ to fit the dynamical magnetic susceptibility of the $pd$-model and found that $U = 5.32t = 2.66$ eV and $t' = 0.06t = 0.03$ eV produce the best agreement between these two models (see Supplementary Note 3).

All of our calculations are performed on $N = 20$ chains (for a total of 80 orbitals total in the multi-orbital case). We have checked that finite-size effects are minimal for chains of this length (see Supplementary Note 4). The simulation temperature was held at $T = 0.0625$ eV for both the single- and multi-orbital DQMC calculations. We also perform simulations for the same system size at $T = 0$ using the DMRG.

**Electronic structure**. There is a significant orbital overlap between the Cu and O orbitals in quasi-1D and 2D cuprate materials, which hybridizes the Cu $3d_{x^2-y^2}$ and O $2p_{x,y}$ orbitals. In the non-interacting limit, these orbitals form bonding ($pd$),

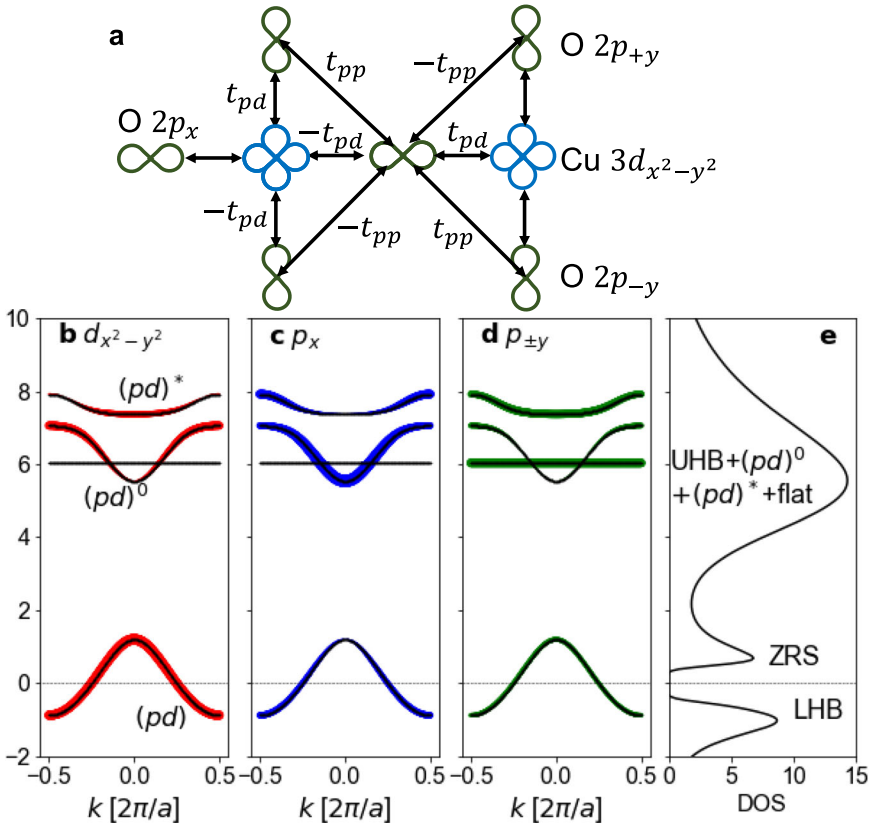


**Fig. 1 The multi-orbital model for the corner-shared cuprate spin chains. a** A sketch of the four-orbital Cu−O *pd*-model describing the corner-shared spin-chain cuprates like $Sr_2CuO_3$. Panels **b**−**d** plot the noninteracting band structure in hole language and at half-filling. In each panel, the weight of the Cu 3*d* and O $2p_x$ and $2p_{\pm y}$ orbitals are indicated by the weight of the colored overlays. Panel **e** shows the density of states (DOS) of the *pd*-model with interactions at half-filling, obtained from determinant quantum Monte Carlo (DQMC) simulations at $T = 0.0625$ eV. Here, LHB (UHB) and ZRS denote the portions of the spectra corresponding to the lower (upper) Hubbard band and the Zhang-Rice Singlet quasi-particle band, while "flat" indicates portions of the electronic structure arising from the non-bonding oxygen $2p_y$ flat band appearing in panel (**d**). The model parameters for the noninteracting bands are the onsite energies $\epsilon_d = 0$, $\epsilon_{p,x} = 3$, and $\epsilon_{p,y} = 3.5$, and the hopping integrals $|t_{(p,x)d}| = 1.5$, $|t_{(p,y)d}| = 1.8$, and $|t_{pp}| = 0.75$. For the DOS shown in panel **e**, we set the onsite Hubbard interactions on Cu and O to $U_d = 8$ and $U_p = 4$, respectively, and the interorbital Cu−O Hubbard interaction to $U_{pd} = 1$. All parameters are given in units of eV.

nonbonding $(pd)^0$, and anti-bonding $(pd)^*$ bands, as shown in Fig. 1b−d. In the corner-shared cuprates, there is also a flat band, which originates from a nonbonding combination of $2p_{\pm y}$ orbitals that does not hybridize with the $3d_{x^2-y^2}$ orbital.

Throughout, we work in hole language where $\langle \hat{n} \rangle = 1$ corresponds to half-filling (i.e., 1 hole/Cu), and $\langle \hat{n} \rangle > 1$ (<1) corresponds to hole (electron) doping. At half-filling, when the interactions are turned on, the bonding (*pd*) band is split into the lower and upper Hubbard band (LHB/UHB) as well as an additional Zhang-Rice band (ZRS) located above the Fermi level[56,57]. These bands can be easily resolved in the total interacting density of states (DOS) shown in Fig. 1e, and in both the single-particle spectral functions shown in Figs. 2 and 3. For our parameters, the energy of the upper Hubbard band is close to the O-derived bands, leading to a broad peak in the DOS centered around $\omega = 6$ eV.

To study the electronic structure of the interacting *pd*-model, we plot the momentum-dependent spectral functions $A(k, \omega)$ in Figs. 2 and 3 for hole concentrations $\langle \hat{n} \rangle = 1.1$, 1, and 0.9. Figures 2a−c and 3a−c show results obtained from finite-temperature DQMC and zero temperature DMRG calculations, respectively. (Additional plots of $A(k, \omega)$ for both models, focusing on the low-energy region $\omega \in [-4,4]$ eV, are provided in Supplementary Note 5.) From bottom to top, the momentum $k$ increases from $-\pi/a$ to $\pi/a$ in each panel. The black dashed lines represent the Fermi level $E_F$. To highlight the orbital content of the spectral features, we indicate the Cu $d_{x^2-y^2}$ orbital of the spectral function with red color and the sum of the spectral weights of the O $p_x$ and O $p_{\pm y}$ orbitals in cyan. The zero-temperature spectral function shown in Fig. 3 exhibits sharper features and hence richer details compared to the DQMC results.

For simplicity, we begin by discussing the spectra at half-filling. Both DQMC and DMRG have a clear gap at the Fermi level $E_F$, consistent with a Mott-insulating state. In the low energy region [−4,4] eV, the DMRG spectra also have footprints of spin-charge separation, consistent with ARPES measurements on $SrCuO_2$[58]. Besides, the DMRG results show a dispersing band between 6 and 8 eV with a significant amount of O 2*p* character and two flat bands at $\omega = 6$ eV and $\omega = 7.2$ eV. The flat band at lower energy is composed almost entirely of the O $2p_{\pm y}$ orbitals and corresponds to the flat band shown in the noninteracting band structure. The higher-energy flat band is mixed between Cu and O and corresponds to the UHB with additional weak Cu satellites at $\omega \approx 10$ eV. Note that the contribution of the Cu orbitals to the anti-bonding $(pd)^*$ band is reduced significantly in the interacting case compared to the noninteracting case. Due to a combination of thermal broadening and the Maximum Entropy method, these fine structures blend into a broad peak in the DQMC results in the same energy region.

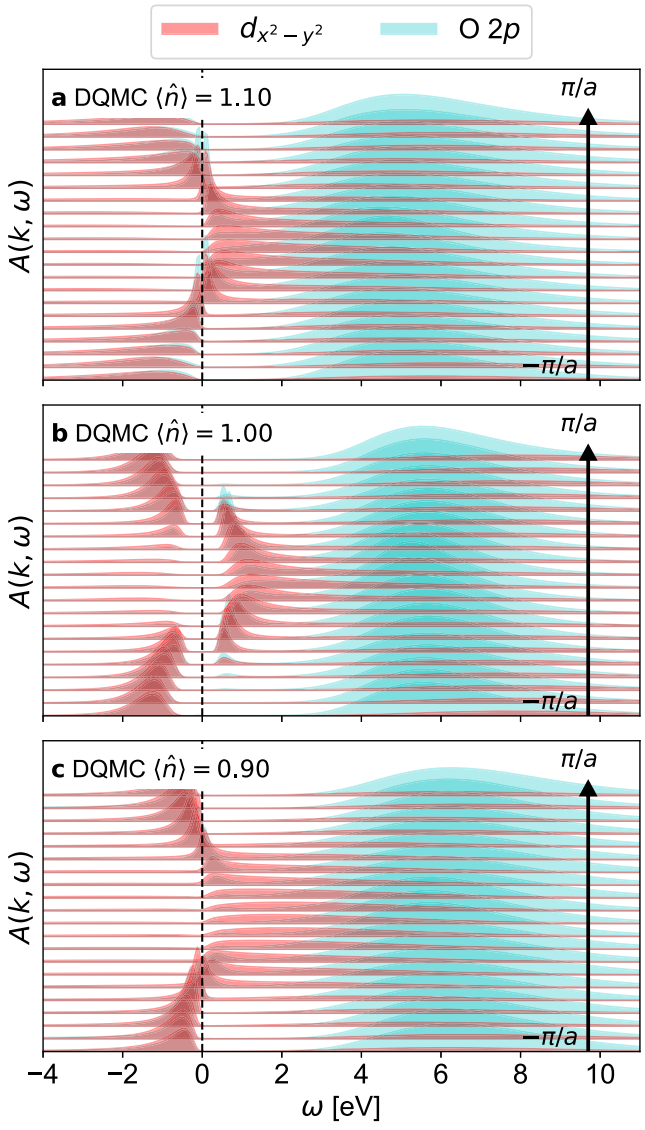


**Fig. 2 The single particle spectral function $A(k,\omega)$ of the multi-orbital model computed using the determinant quantum Monte Carlo (DQMC) method.** Results are shown as a function of momentum $k$ and energy $\omega$ for fillings of **a** $\langle\hat{n}\rangle = 1.1$, **b** $\langle\hat{n}\rangle = 1$, and **c** $\langle\hat{n}\rangle = 0.9$ holes/Cu. Red color represents Cu $d_{x^2-y^2}$, while cyan color represent the sum of O $p_x$ and O $p_{\pm y}$ components. From bottom to top, the momentum $k$ increases from $-\pi/a$ to $\pi/a$ in each panel. All results were obtained on chains with $N = 20$ unit cells and onsite energies $\epsilon_d = 0$, $\epsilon_{p,x} = 3$, and $\epsilon_{p,y} = 3.5$, hopping integrals $|t_{\langle p,x\rangle d}| = 1.5$, $|t_{\langle p,y\rangle d}| = 1.8$, and $|t_{pp}| = 0.75$, and Hubbard interactions $U_d = 8$, $U_p = 4$, and $U_{pd} = 1$, in units of eV.

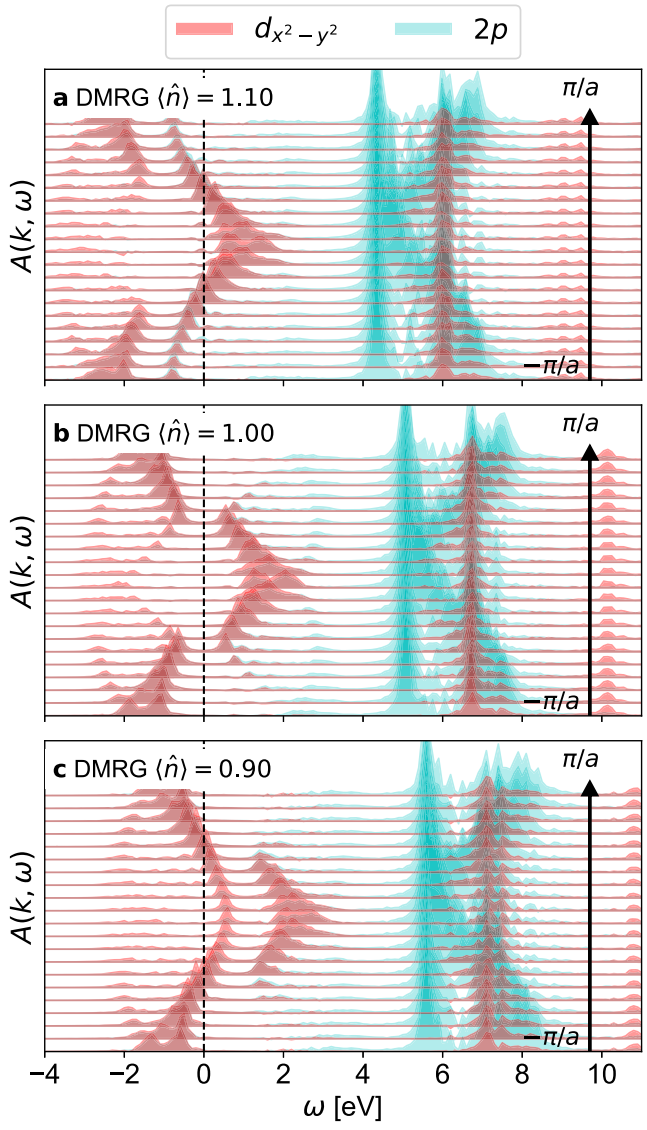


**Fig. 3 The single particle spectral function $A(k,\omega)$ of the multi-orbital model computed using the density matrix renormalization group (DMRG) method.** Results are shown as a function of momentum $k$ and energy $\omega$ for fillings of **a** $\langle\hat{n}\rangle = 1.1$, **b** $\langle\hat{n}\rangle = 1$, and **c** $\langle\hat{n}\rangle = 0.9$ holes/Cu. Red color represents Cu $d_{x^2-y^2}$, while cyan color represents the sum of O $p_x$ and O $p_{\pm y}$ components. From bottom to top, the momentum $k$ increases from $-\pi/a$ to $\pi/a$ in each panel. All results were obtained on chains with $N = 20$ unit cells and onsite energies $\epsilon_d = 0$, $\epsilon_{p,x} = 3$, and $\epsilon_{p,y} = 3.5$, hopping integrals $|t_{\langle p,x\rangle d}| = 1.5$, $|t_{\langle p,y\rangle d}| = 1.8$, and $|t_{pp}| = 0.75$, and Hubbard interactions $U_d = 8$, $U_p = 4$, and $U_{pd} = 1$, in units of eV.

By considering the full *pd*-model, we can access the Cu and O components to the spinon and holon states in the low energy region, which have not been reported in the literature to our knowledge. Our DMRG results show that the Cu and O weights of the main structures are comparable over the entire Brillouin zone. We note, however, that the holon-shadow bands are dominated by the Cu component below the Fermi level near $k = 0$ but dominated by the O component above the Fermi level near $k = \pm\pi/a$. Our DQMC results show a similar composition for the main structures, but the intensity of the shadow bands is too weak to be captured by our Maximum Entropy method.

The system undergoes a metal−insulator transition as the system is either electron- or hole-doped. In our *pd*-model, we see that spinon-antiholon branches are responsible for the spectral weight crossing the Fermi level, consistent with the results of the single-band Hubbard model[59]. The orbital components in both low and high-energy regions do not change much compared to the half-filled case.

**The magnetic excitations**. We now examine the collective magnetic excitations of the *pd*-model. Figure 4a−j summarizes our finite-temperature ($T = 0.0625$ eV) DQMC results for the dynamical spin structure factor $S(q,\omega)$ for doping levels spanning from $\langle\hat{n}\rangle = 0.8-1.2$. (Additional DQMC data for the doping levels not shown here are provided in Supplementary Note 6.) Figure 5a−j shows comparable results at zero temperature

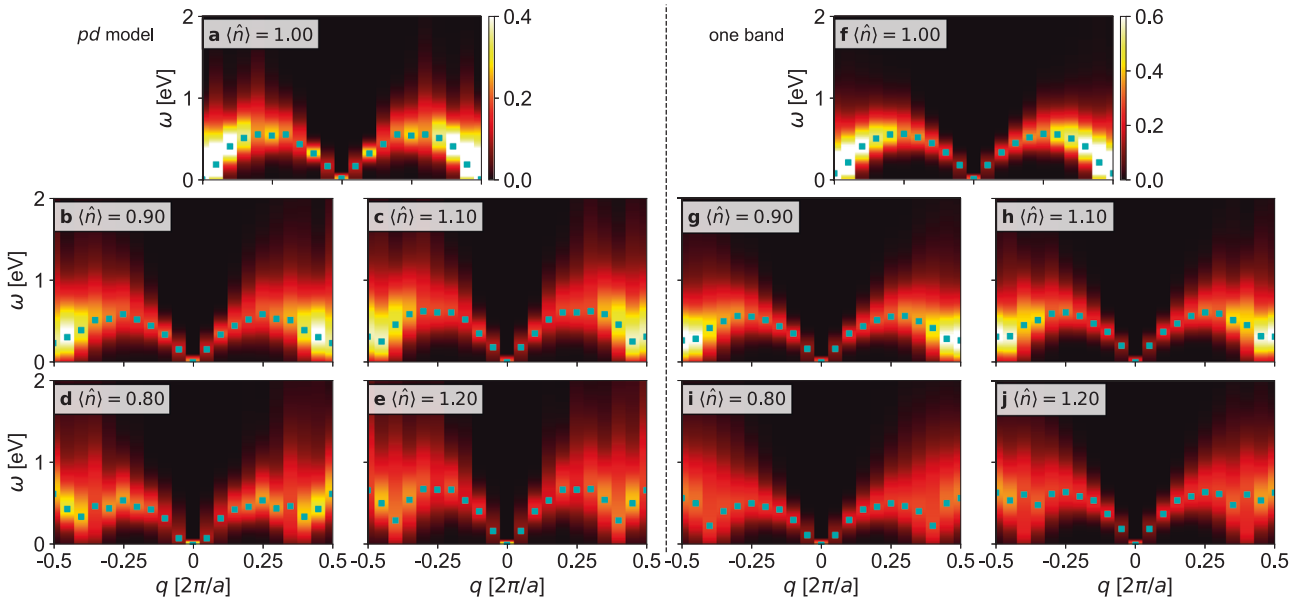


**Fig. 4 Finite temperature determinant quantum Monte Carlo (DQMC) results for the total dynamical spin structure factor $S(q, \omega)$ of the multi-orbital *pd*- and single-band Hubbard models.** Panels **a**–**e** show the dynamical spin structure factor $S(q, \omega)$ as a function of momentum $q$ and energy $\omega$, obtained from DQMC simulations of the multi-orbital model with a Cu−O basis (the *pd*-model) at various fillings $\langle \hat{n} \rangle$, as indicated. The parameters for the *pd*-model include the onsite energies $\epsilon_d = 0$, $\epsilon_{p,x} = 3$, and $\epsilon_{p,y} = 3.5$, the hopping integrals $|t_{\langle p,x \rangle d}| = 1.5$, $|t_{\langle p,y \rangle d}| = 1.8$, and $|t_{pp}| = 0.75$, onsite Hubbard interactions $U_d = 8$ and $U_p = 4$, and the interorbital Hubbard interaction $U_{pd} = 1$, in units of eV. Panels **f**–**j** show corresponding results for DQMC simulations of the single-band Hubbard model with nearest-neighbor hopping $t = 0.5$ eV, next-nearest-neighbor hopping $t' = 0.06t = 0.03$ eV, and an onsite Hubbard interaction $U = 5.32t = 2.66$ eV. Both sets of results were obtained using chains with $N = 20$ unit cells and at temperature $T = 0.0625$ eV.

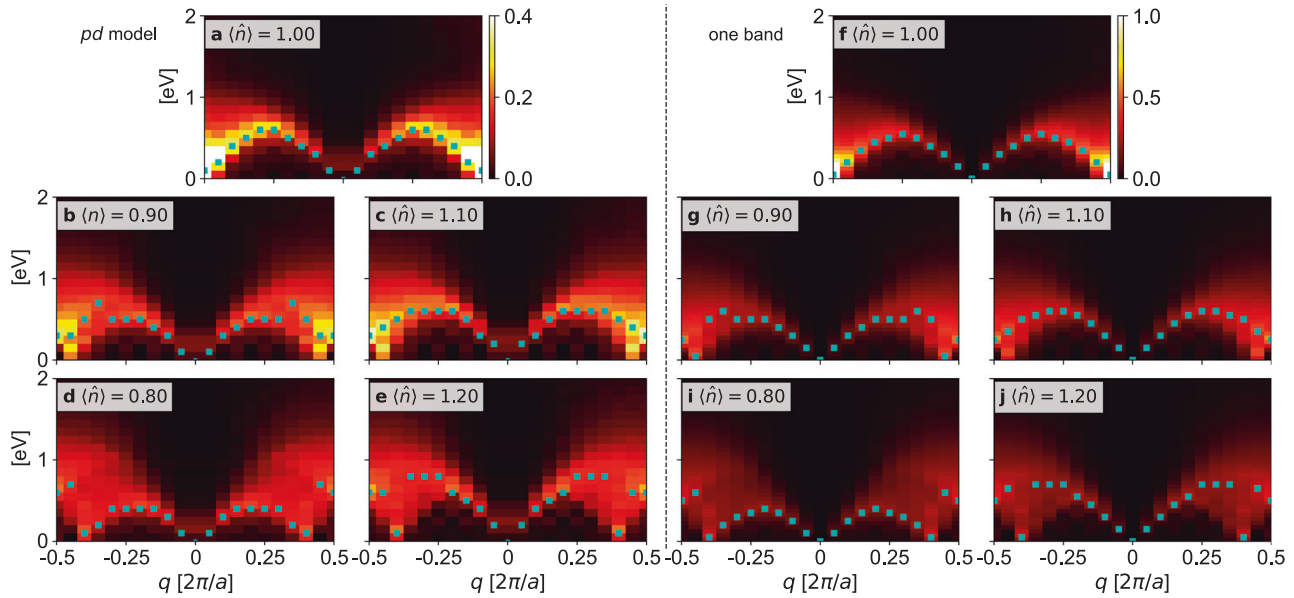


**Fig. 5 Zero temperature density matrix renormalization group (DMRG) results for the total dynamical spin structure factor $S(q, \omega)$ of the multi-orbital *pd*- and single-band Hubbard models.** Panels **a**–**e** show the dynamical spin structure $S(q, \omega)$ as a function of momentum $q$ and energy $\omega$, obtained from DMRG simulations of the multi-orbital model with a Cu−O basis (the *pd*-model) at various fillings $\langle \hat{n} \rangle$, as indicated. The parameters for the *pd*-model include the onsite energies $\epsilon_d = 0$, $\epsilon_{p,x} = 3$, and $\epsilon_{p,y} = 3.5$, the hopping integrals $|t_{\langle p,x \rangle d}| = 1.5$, $|t_{\langle p,y \rangle d}| = 1.8$, and $|t_{pp}| = 0.75$, onsite Hubbard interactions $U_d = 8$ and $U_p = 4$, and the interorbital Hubbard interaction $U_{pd} = 1$, in units of eV. Panels **f**–**j** show corresponding results for DMRG simulations of the single-band Hubbard model with nearest-neighbor hopping $t = 0.5$ eV, next-nearest-neighbor hopping $t' = 0.06t = 0.03$ eV, and an onsite Hubbard interaction $U = 5.32t = 2.66$ eV. Both sets of results were obtained using chains with $N = 20$ unit cells and at zero temperature.

obtained using DMRG. In both Figs. 4 and 5, panels a–e show the spectra obtained from the full *pd*-model while panels f–j show the corresponding results obtained from a single-band Hubbard model. To compare to the single-band model, we present the total spin response of the *pd*-model. We stress that both the cluster sizes and simulation temperatures are the same for the two models, and one can directly compare the results shown on both sides of each figure.

At low-temperature and $\langle \hat{n} \rangle = 1$, the corner-shared cuprates are charge-transfer insulators with antiferromagnetic correlations.

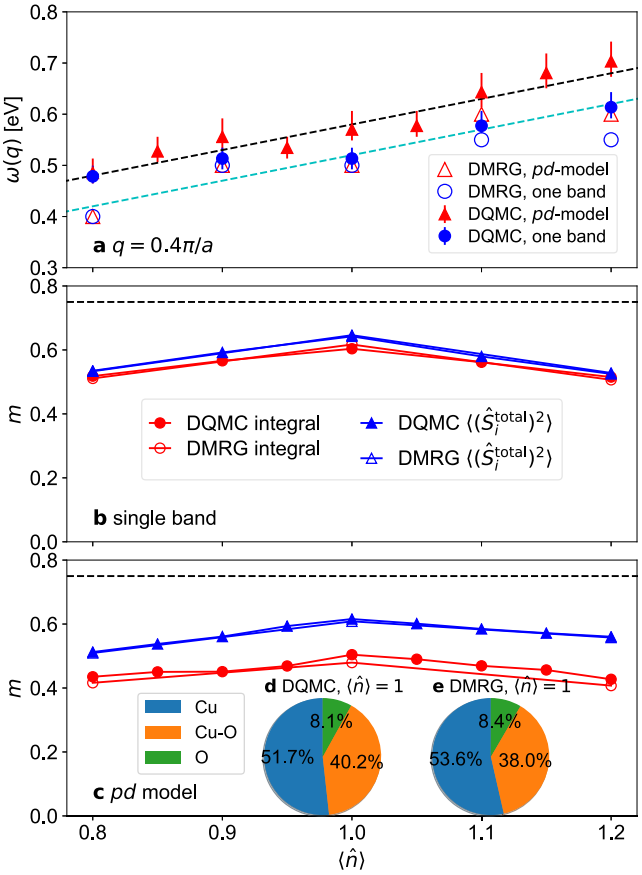


**Fig. 6 The evolution of the magnetic moment and excitations with doping $\langle\hat{n}\rangle$.** **a** The shift in energy $\omega(q)$ of the maximum of $S(q = 0.4\pi/a, \omega)$ as a function of doping in the multi-orbital Cu−O *pd*- and single-band models. The dashed lines are guides to the eye. Panels **b**, **c** show the evolution of the magnetic moment in the single-band (panel **b**) and *pd*-models (panel **c**). The blue triangles indicate the value of $m$ estimated by computing the expectation value of the local spin operator $\langle(\hat{S}_i^{\text{total}})^2\rangle$ while the red circles indicate the value of $m$ estimated by integrating $S(q, \omega)$ from $\omega \in [0, 3]$ eV. Results are shown for determinant quantum Monte Carlo (DQMC) simulations at $T = 0.0625$ eV and density matrix renormalization group (DMRG) simulations at zero temperature. The pie charts insets show the weight of the Cu, O, and Cu−O components of the moment calculated using **d** DQMC and **e** DMRG (see "Methods").

The system's elementary magnetic excitations are spinons in this limit, which must be created in pairs. The magnetic excitation spectrum is dominated by a two-spinon continuum, which has been explicitly observed in, for example, $Sr_2CuO_3$ using INS[43] and RIXS[45,46]. The upper and lower boundaries of the two-spinon continuum are given by $\omega_+(q) = \pi J|\sin(qa/2)|$ and $\omega_-(q) = \frac{\pi J}{2}|\sin(qa)|$, respectively, where $J$ is the Cu−Cu antiferromagnetic superexchange energy. Our DQMC and DMRG results for both the *pd*- (Figs. 4a and 5a) and single-band (Figs. 4f and 5f) models reproduce this behavior. Specifically, we observe a continuum of magnetic excitations confined within $\omega_\pm(q)$ but with a maximum spectral weight $\omega_m(q)$ [indicated by the cyan points] concentrated at energies near the lower boundary $\omega_-(q)$. This distribution suggests that the low-energy magnetic excitations of the *pd*-model are close to the Heisenberg limit, where the low-energy physics is described by the 1D *t*-*J* model[55,60]. By assuming that the locations of the maximum spectral weight in Figs. 4a and 5a correspond to $\omega_-(q)$, we can estimate $J = \frac{2}{\pi}\omega_m/\sin(\frac{\pi}{2}) \approx 350$ meV for the multi-orbital model. This value is a little smaller than the value $J \approx 4t^2/U = 376$ meV that one would obtain from the single-band Hubbard model in the large $U$ limit. (For this estimate, we have neglected the presence of $t' = 0.06t$, which would induce a negligible frustration to the system.)

Upon doping $\langle\hat{n}\rangle = 1 + x$, the location of the zero-energy mode $q_s$ shifts from $\frac{\pi}{a}$ to $(1 - |x|)\frac{\pi}{a}$, consistent with the prior demonstration that the deviation of the wave vector from $\pi/a$ is proportional to the excess hole or electron concentration[60]. We note that using DQMC, at the largest doping, $|x| = 0.2$, the spin excitations at $q_s = 0.8\frac{\pi}{a}$ appear to acquire a finite gap at $T = 0.0625$ eV but remain gapless at zero temperature. This behavior may be an artifact of the Maximum Entropy Method and/or the finite temperature effect of the simulation.

We observe a hardening of the spin excitation spectrum as the total hole concentration increases. For example, Fig. 6a shows the change of the energy of the maximum intensity $I_{\max}(q)$ of $S(q, \omega)$ as a function of the hole density at $q = 0.4\pi/a$. Here, the solid triangles and circles represent DQMC results, while the open triangles and circles represent DMRG results. Since the DQMC data can be broad due to thermal broadening and the use of the Maximum Entropy method, we also provide approximate error bars, which are estimated as the energy range over which $S(q, \omega) \geq 0.99 I_{\max}(q)$. The two dashed lines are guides to the eye. For both the *pd*- and downfolded single-band models, we find that the energy of the peak increases with $\langle\hat{n}\rangle$. This observation implies that the spin excitation energy hardens with hole-doping and softens with electron doping. We also note that the spin excitations obtained with DQMC at finite temperature are slightly higher in energy compared to the DMRG results, implying that the spin excitations shift to higher energies as the temperature increases.

The observed particle−hole asymmetry in the energy scale of the magnetic excitations is opposite to what is found in the two-dimensional Hubbard model and experimental observations for the 2D cuprates[18,20]. Since we observe consistent behavior in our 1D single- and multi-orbital models, we attribute this difference to the value of $t'$ used in the models. For example, ref. 18 showed that the single-band Hubbard model could account for the observed behavior in 2D, provided $t' \approx -0.3t$. Similarly, ref. 61 reported that the spin excitations in a 1D single-band Hubbard model harden in the electron-doped case and soften significantly in the hole-doped case after assuming $t' = -0.3t$ to remain consistent with the 2D cuprates. Later, ref. 62 showed that changing the sign of $t'$ reverses this behavior in 1D, consistent with our current results. It is important to stress that the next-nearest-neighbor hopping process $t'$ in the 1D case is actually analogous to the next-next-nearest-neighbor process $t''$ in the 2D cuprates. With this in mind, it is then natural to expect that the value of $t'$ in 1D will be very different from the one found in 2D with $|t'_{1D}| \approx |t''_{2D}| < |t'_{2D}|$. We circumvent this issue by comparing the single-band description directly to the multi-orbital description, where explicitly determining the value of $t'$ is not needed. To reproduce the multi-orbital behavior, we found that $t' = 0.06t > 0$, in line with our expectations that $|t'_{1D}| < |t'_{2D}|$.

In the strong coupling limit, the magnetic moment $m = \sqrt{S(S+1)} = 0.75$ in the single-band Hubbard model; however, this value will be reduced for finite $U$ due to double occupancy and additional covalency effects in the *pd*-model[43]. To determine by how much, we calculated the local moment from the expectation value of the local spin operator $m = \langle(\hat{S}_i^{\text{total}})^2\rangle$, where $\hat{S}_i^{\text{total}} = \hat{S}_i$ and $\hat{S}_i^{\text{total}} = \sum_\alpha \hat{S}_{i,\alpha}$ measures the total spin in the unit cell for the single and multi-orbital models, respectively. The results are shown in Fig. 6b, c for the single- and multi-band cases,

respectively. For both models, the DMRG and DQMC results are in excellent agreement and predict an average local moment $m \approx 0.6$ at half-filling, which decreases as the system is doped with electrons or holes. This decrease is mostly symmetric in the single-band case and slightly asymmetric in the multi-band case. Besides, we note that the temperature used in our DQMC simulations is low enough so that the local magnetic moment is the same as that at zero temperature. These results imply that the effective moment in both models has a slight reduction due to double occupancy, consistent with previous INS studies[43,44,63].

We can also estimate the effective size of the system's local moment using a sum rule that relates it to an integral over the spin structure factor

$$m = \lim_{\omega_c \to \infty} \frac{3}{N} \sum_{\alpha,\beta,q} \int_0^{\omega_c} S^{\alpha,\beta}(q,\omega) e^{iq(r_{x,\alpha} - r_{x,\beta})} d\omega. \quad (3)$$

Here, $N$ is the number of the unit cells, $\alpha$, $\beta$ are orbital indices, $r_{x,\alpha}$ and $r_{x,\beta}$ are the $x$-components of the basis vectors, and the factor of three comes from the sum over the three spin components, which contribute equally because of the unbroken SU(2) symmetry. Since INS experiments typically only access the low energy region, in practice, one needs to cut off the integration to a finite value of $\omega_c$ (= 3 eV in our case). Performing the integral for the single-band case, we find that the total sum rule is almost completely recovered. However, for the *pd*-model, this energy window only recovers ≈ 75−80% of the sum rule, depending on the doping. This discrepancy is not due to the use of the Maximum Entropy method, as we obtain very consistent results using DMRG and DQMC. Rather, it reflects that some of the magnetic moment has been transferred to higher energies in the *pd*-model. To verify this, we also computed $S(q,\omega)$ to high energies and confirmed that extending to $\omega_c = 13$ eV recovers the missing weight (see Supplementary Note 7). Reference 43 previously estimated the local moment in $Sr_2CuO_3$ by integrating INS data for $S(q,w)$ up to $\omega_c = 1$ eV. The authors were only able to recover 80% of the sum rule after accounting for covalency effects and attributed the missing weight to Debye−Waller effects. Our results demonstrate that the missing weight has instead been transferred to higher energies. Remarkably, the magnetic excitations of the full multi-orbital are well reproduced by our effective single-band model, even though ≈20% of the overall magnetic moment is transferred to higher energies in the *pd*-model.

Next, we analyze the contribution of each orbital to the total magnetic moment. The inset of Fig. 6c plots the weight of spin excitations between two Cu orbitals, two O orbitals, and Cu and O orbitals at half-filling. Here, the intraorbital spin excitations between neighboring Cu and O orbitals are labeled as "Cu" and "O," respectively, while interorbital spin excitations between Cu and O are labeled as "Cu−O". Interestingly, we observe that the spin excitations on the Cu sites have the maximum weight (about 52%), and interorbital spin excitations between Cu and O account for sizable 39% of the total excitations.

**The charge excitations**. We now examine the charge excitations of the *pd*-model and compare them to the excitations predicted by the single-band model. Figure 7 plots DQMC results for the dynamical charge structure factor $N(q,\omega)$ obtained from both models, again at $T = 0.0625$ eV and for different hole densities. As was the case with our spin results, $N(q,\omega)$ represents the total charge response, and panels a−e show the excitation spectrum of the *pd*-model while panels f−j show the excitation spectrum of the single-band Hubbard model. Figure 8 plots DMRG results for the same models at zero temperature, following the same format.

The charge excitation spectrum of the *pd*-model can be divided into low- and high-energy sectors, with dividing line occurring at $\omega \approx 5$ eV, as shown in Figs. 7 and 8. The high-energy region corresponds to particle−hole excitations from the low-energy bands crossing $E_F$ to the high-energy oxygen-derived bands and UHB observed in the spectral function. The charge excitations in the low-energy region appear as a sharp cosine-like excitation that is gapped at half-filling and gapless in the doped systems. These low-energy features originate from scattering within holon and ZRS bands near the Fermi level.

At zero temperature, shown in Fig. 8, additional fine structure in the high- and low-energy regions of the spectral function develops. Here, we observe that the low-energy region consists of two distinct branches, one gapped and the other gapless. The gapless excitations are intraband scattering within the holon branch of the doped system and are notably absent in the spectra at half-filling. The gapped excitations are then scattering from the holon band to the remnant of the ZRS band (located at $\omega \in [-3,-1]$ eV in Fig. 3a and $\omega \in [1, 4]$ eV in Fig. 3c, respectively).

When comparing our *pd*-model results to the single-band model, we focus on the low-energy section of the charge excitation spectrum because the high-energy excitations are understandably absent in the single-band model. Overall, we find that the low-energy charge excitations of the *pd*-model are qualitatively well described by the single-band model. The DMRG results show that both the single-band and *pd*-models have gapped and gapless charge excitations when $\langle \hat{n} \rangle \neq 1$. The gapped excitations of the single-band model originate from the scattering between the holon band and the upper Hubbard band, while these gapped excitations of the *pd*-model come from the scattering between the holon band and the remnant ZRS band. In the DQMC results, due to the broadening of the finite temperature and the Maximum Entropy method, the sharp gapped spectrum is replaced by a broad spectrum, connecting to the spectrum of the gapless excitation.

To better visualize the charge excitations of the DQMC results at low- and high-energy, we plot $N(q,\omega)$ of the *pd*-model in Fig. 9 for $\langle \hat{n} \rangle = 0.9$, $\langle \hat{n} \rangle = 1.1$, $\langle \hat{n} \rangle = 0.8$, and $\langle \hat{n} \rangle = 1.2$ at $q = \pi/a$. We also include the DMRG results for reference. We decomposed the DQMC results into three Gaussian functions to distinguish the low- and high-energy charge excitations. The centers of these three Gaussian functions coincide with the peak position of the DMRG results. The sum of these three Gaussian functions matches the original DQMC results very well. Besides, we observe an asymmetry in the intensity of the lowest energy peak between hole- and electron-doped regimes consistent with the asymmetric orbital content between Cu and O in the undoped ground state.

Even though the single-band model can describe the low-energy total charge excitations, the orbital-resolved results show a fascinating behavior, which could help account for the particle-hole asymmetry observed in RIXS experiments[64,65]. Figure 10 shows the orbital-resolved $N^{\gamma,\gamma'}(q,\omega)$, which is evaluated from both DMRG and DQMC calculations. Red, cyan, and blue colors in Fig. 10 represent the charge excitations between Cu−Cu, O−O, and Cu−O, respectively. We observe that the gapless low-energy charge excitation for $\langle \hat{n} \rangle = 0.9$ is dominated by the Cu−Cu and Cu−O components, while the similar charge excitation for $\langle \hat{n} \rangle = 1.1$ mainly consists of the O−O and Cu−O components. In two-dimensional superconducting cuprates, Cu $L_3$-edge RIXS experiments reported a strong charge signal near $q = 0$ on the electron-doped side, which has been difficult to observe on the hole-doped side[64,65]. The missing signal with hole doping may be attributed to the weaker contribution to the charge excitations originating from the Cu−Cu excitations. Our

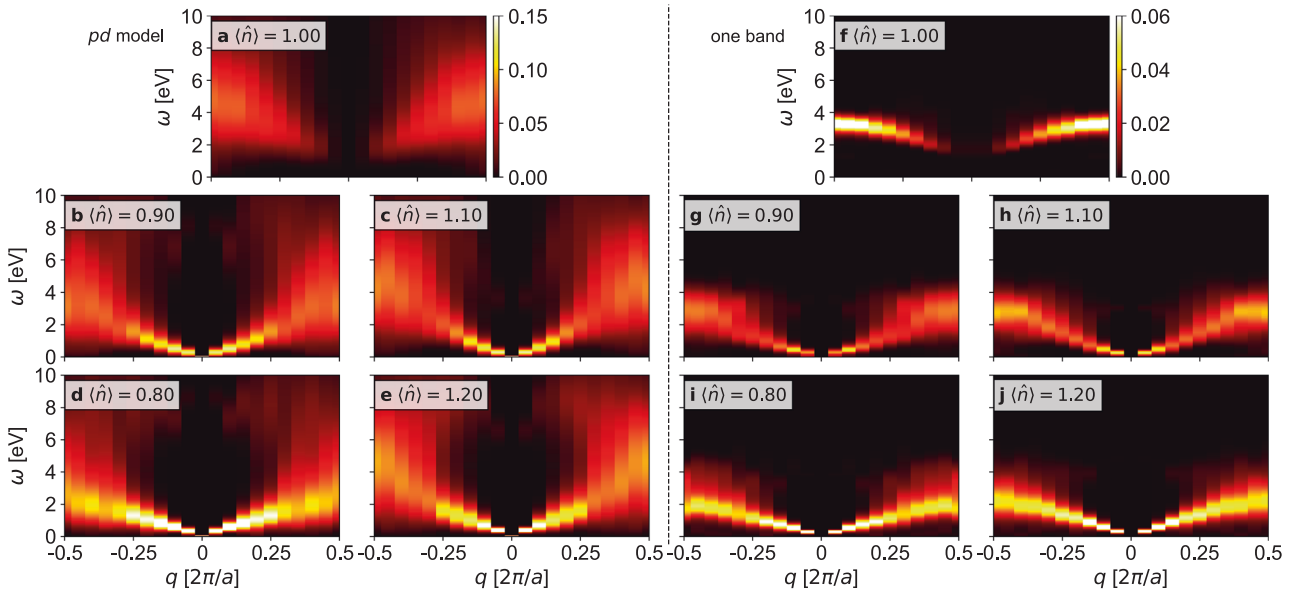


**Fig. 7 Finite temperature determinant quantum Monte Carlo (DQMC) results for the total dynamical charge structure factor $N(q, \omega)$ of the multi-orbital *pd*- and single-band Hubbard models.** Panels **a**–**e** show the dynamical charge structure $N(q, \omega)$ as a function of momentum $q$ and energy $\omega$, obtained from DQMC simulations of the multi-orbital with a Cu−O basis (the *pd*-model) at various fillings $\langle \hat{n} \rangle$, as indicated. Panels **f**–**j** show corresponding results for DQMC simulations of the single-band Hubbard model. Both sets of results were obtained using chains with $N = 20$ unit cells and at temperature $T = 0.0625$ eV. The model parameters are identical to those used in Fig. 4.

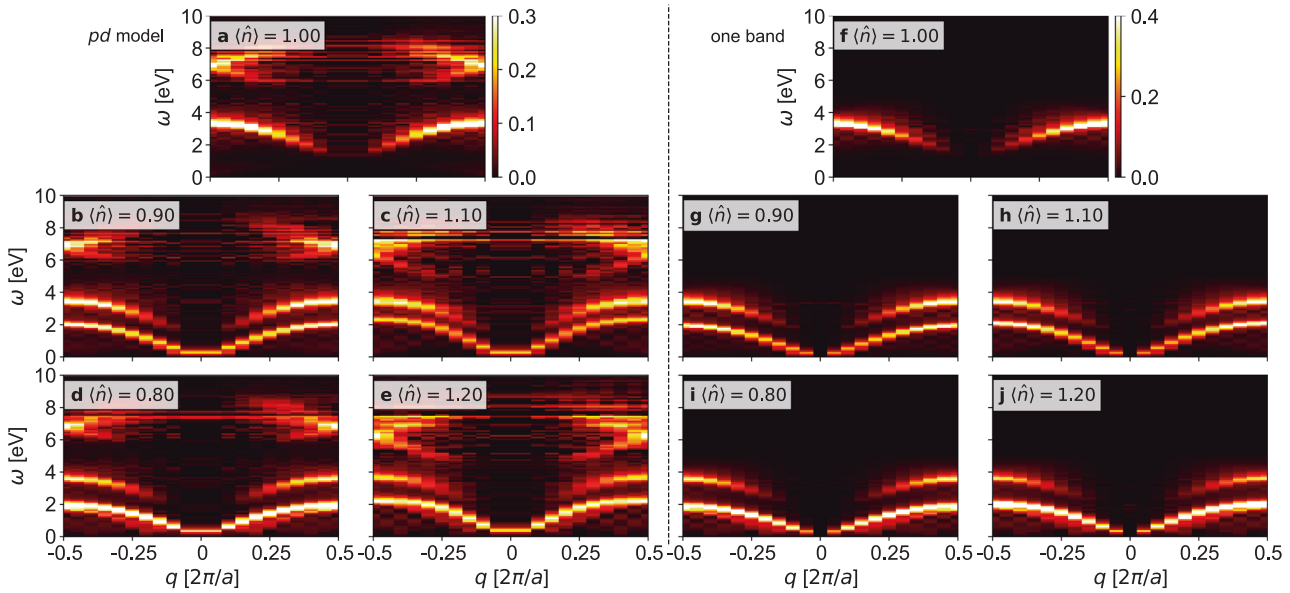


**Fig. 8 Zero temperature density matrix renormalization group (DMRG) method results for the total dynamical charge structure factor $N(q, \omega)$ of the multi-orbital *pd*- and single-band Hubbard models.** Panels **a**–**e** show the dynamical charge structure factor $N(q, \omega)$ as a function of momentum $q$ and energy $\omega$, obtained from DMRG simulations of the multi-orbital with a Cu−O basis (the *pd*-model) at various fillings $\langle \hat{n} \rangle$, as indicated. Panels **f**–**j** show corresponding results for DMRG simulations of the single-band Hubbard model. Both sets of results were obtained using chains with $N = 20$ unit cells. The model parameters are identical to those used in Fig. 5.

results show that the lost signal can be observed in the O components, consistent with the O *K*-edge RIXS results.

## Conclusion

We have studied the dynamical spin and charge structure factors of a four-orbital *pd*-model relevant for one-dimensional cuprate spin chains using numerically exact DQMC, DMRG, and ED. We also compared the two-particle response functions of the *pd*-model against those predicted by an effective downfolded single-band Hubbard model.

Our results show that the single-band Hubbard model can describe the low-energy total spin and charge excitations of the *pd*-model upon hole- or electron-doping. In the case of the magnetic excitations, we found that the collective excitations harden (soften) with hole (electron) doping. This asymmetry is captured by the single-band Hubbard model with a small positive hopping between next-nearest-neighbors. We find even richer physics in our orbital-resolved results in the four-orbital *pd*-model. For example, we find that the low-energy spin excitations mainly consist of intraorbital Cu−Cu and interorbital Cu−O

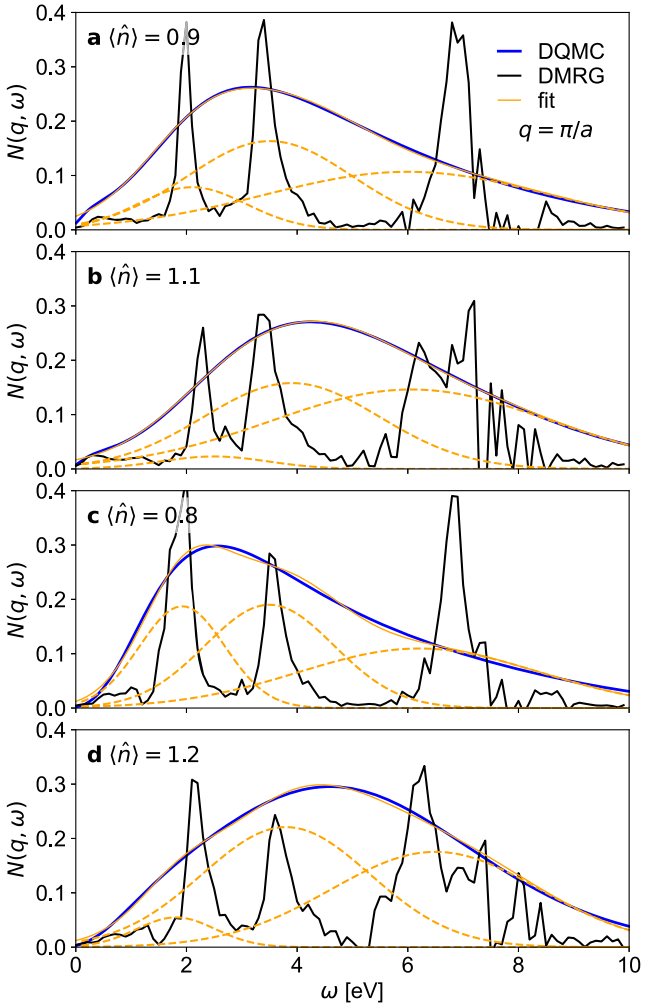


**Fig. 9 Comparative analysis of the charge excitations in the Cu−O *pd*-model.** Results were obtained using the determinant quantum Monte Carlo (DQMC) and density matrix renormalization group (DMRG) methods. Panels **a**–**d** show the dynamical charge structure factor $N(q,\omega)$ as a function of energy $\omega$ at $q=\pi/a$ for fillings of **a** $\langle\hat{n}\rangle=0.9$, **b** $\langle\hat{n}\rangle=1.1$, **c** $\langle\hat{n}\rangle=0.8$, and **d** $\hat{n}=1.2$, respectively. The DQMC spectra (blue line) have been fit with a set of Gaussian distributions, whose energies correspond well with the main peaks observed in the DMRG data (black line). The parameters for the *pd*-model, which includes the full Cu and O basis, are identical to those used in Figs. 4 and 5.

components, and we distinguish the dynamical spin behaviors on each orbital, including the effects of electron−electron interactions beyond first principle approaches[43]. Our observations for the collective charge excitations, which have not been widely studied in the context of cuprate physics, are richer. Our results show a gapped charge excitation spectrum in the undoped regime. In contrast, gapless excitations develop upon doping with weaker intensity on the hole-doped side than on the electron-doped side at low energy. In the low-energy sector, the charge excitations in the electron-doped regime are dominated by the Cu−Cu and Cu−O components, while in the hole-doped regime they are dominated by the Cu−O and O−O components. This behavior reflects the charge transfer insulating nature of the cuprates, where doped holes preferentially reside on the oxygen sublattice while doped electrons reside on the copper sublattice.

Our work has important implications for numerical studies of competing and intertwined orders in one- and two-dimensional cuprates. For example, in the 2D superconducting cuprates, a clear particle-hole asymmetry has been identified in the excitations probed by RIXS experiments[64,65]. Here, a branch of collective modes has been observed in the electron-doped $Nd_{2-x}Ce_xCuO_4$, which has been challenging to observe in hole-doped cuprates. This particle-hole asymmetry of the collective modes is consistent with the behaviors of the charge excitations on the Cu site observed here, suggesting that the explicit inclusion of the oxygen degrees of freedom may be required to capture this physics. It would, therefore, be interesting to extend this study to higher dimensions by considering multi-leg ladders on the route towards full 2D models. Finally, our results provide extensive predictions for the evolution of the spin and charge excitations in doped cuprate spin chains, which have been synthesized recently for a wide range of hole doping[37].

## Methods

**Determinant quantum Monte Carlo**. The details of the DQMC algorithm applied to the multi-orbital Hubbard models can be found in ref. 66. DQMC works in the grand canonical ensemble, where the expectation value of an observable $\hat{O}$ is given by $\langle\hat{O}\rangle=Z^{-1}\mathrm{Tr}[\hat{O}e^{-\beta H}]$, where $Z=\mathrm{Tr}[e^{-\beta H}]$ is the partition function and $\beta$ is the inverse temperature.

To study the model's excited state properties, we measured the imaginary-time dynamical magnetic $\chi_s$ and charge $\chi_c$ susceptibilities. They are given by

$$\chi_s^{\gamma,\gamma'}(q,\tau)=\langle\hat{S}_q^{\gamma,z}(\tau)\hat{S}_{-q}^{\gamma',z}(0)\rangle \tag{4}$$

and

$$\chi_c^{\gamma,\gamma'}(q,\tau)=\langle\hat{n}_q^{\gamma}(\tau)\hat{n}_{-q}^{\gamma'}(0)\rangle, \tag{5}$$

where $\hat{S}_q^{\gamma,z}(\tau)=\hat{n}_{q,\uparrow}^{\gamma}(\tau)-\hat{n}_{q,\downarrow}^{\gamma}(\tau)$ and $\hat{n}_q^{\gamma}(\tau)=\hat{n}_{q,\uparrow}^{\gamma}(\tau)+\hat{n}_{q,\downarrow}^{\gamma}(\tau)$. Here, $\gamma$ ($\gamma'$) is the orbital index, and $\hat{n}_{q,\sigma}^{\gamma}$ and $\hat{S}_q^{\gamma,z}$ are the Fourier transforms of the local density and spin-$z$ operators.

To compare to the single-band model, we calculate the total spin and charge responses, which are given by

$$\chi_s(q,\tau)=\langle\hat{S}_q^{z}(\tau)\hat{S}_{-q}^{z}(0)\rangle \tag{6}$$

and

$$\chi_c(q,\tau)=\langle\hat{n}_q^{z}(\tau)\hat{n}_{-q}^{z}(0)\rangle, \tag{7}$$

where $\hat{S}_q^z=\sum_{i,\gamma}e^{iqr_{i,\gamma}}\hat{S}_{i,\gamma}^z$ and $\hat{n}_q^z=\sum_{i,\gamma}e^{iqr_{i,\gamma}}\hat{n}_{i,\gamma}$. Here, $r_{i,\gamma}$ represents the position of the orbital $\gamma$. Besides, we also calculate the spin and charge responses between Cu (O) and O sites, where the operator on the O site is given by $\hat{O}=\hat{O}_{p_x}+\hat{O}_{p_y}+\hat{O}_{p_{-y}}$.

To examine the spectral properties, we then used the method of the maximum of entropy[67] to analytically continue the imaginary-time susceptibilities to the real frequency axis. Some of the authors have used the same analytic continuation method to study the 2D cuprates, and reasonable results were obtained[20]. The dynamical spin and charge structure factors are calculated by the fluctuation-dissipation theorem, which simplifies to

$$S^{\gamma,\gamma'}(q,\omega)=\frac{\mathrm{Im}\chi_s^{\gamma,\gamma'}(q,\omega)}{1-e^{-\beta\omega}} \tag{8}$$

and

$$N^{\gamma,\gamma'}(q,\omega)=\frac{\mathrm{Im}\chi_c^{\gamma,\gamma'}(q,\omega)}{1-e^{-\beta\omega}}. \tag{9}$$

The primary drawback to DQMC is the Fermion sign problem[68], which limits the range of accessible temperatures and Hubbard interactions. In general, we have found that the sign problem is alleviated in 1D systems[38], and the smallest value of the sign we obtained in our simulations is about 0.78, much larger than the sign value of the 2D three-orbital *pd*-model[29].

**Density matrix renormalization group**. The DMRG[69,70] calculations were carried out with the correction-vector method[39] using the Krylov decomposition[40], as implemented in the DMRG++ code[71]. This approach requires real-space representations for the dynamical structure factors in Eqs. (4) and (5), which can be found in ref. 72. Here, we calculated the response functions for $N=20$ unit cell long chains with open boundary conditions, corresponding to total system sizes of $N$ and $4N+1$ orbitals for the single- and multi-orbital cases, respectively. We kept up to $m=1000$ DMRG states to maintain a truncation error below $10^{-7}$ and introduced a spectral broadening in the correction-vector approach fixed at $\eta=0.1$ eV for both the single- and multi-band calculations. We note that the accuracy of our calculation deteriorates at high excitation energies even with such small truncation errors.

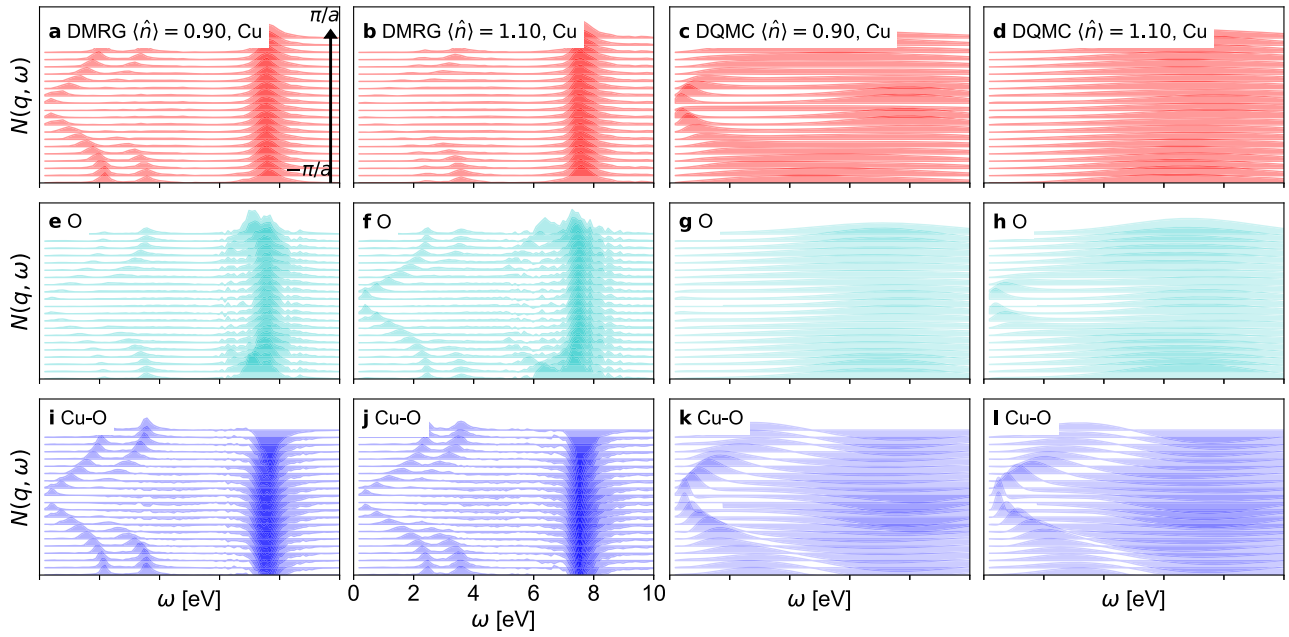


**Fig. 10 The orbital-resolved dynamical charge structure factor $N(q,\omega)$ of the Cu−O *pd*-model.** Results were computed using the density matrix renormalization group (DMRG) and determinant quantum Monte Carlo (DQMC) methods. Panels **a**–**l** show results as a function of energy $\omega$ for filling values of $\langle\hat{n}\rangle = 0.9$ and 1.1 holes/Cu. Red, cyan, and blue colors represent Cu $d_{x^2-y^2}$, O 2*p*, and Cu−O components, respectively. From bottom to top, the momentum $q$ increases from $-\pi/a$ to $\pi/a$ in each panel. The parameters for the *pd*-model, which includes the full Cu and O basis, in both cases, are identical to those used in Figs. 4 and 5.

This behavior is expected within our Krylov DMRG correction vector approach, as introduced in ref. 40. In the Krylov method, another source of error is given by the Lanczos error, which occurs in the tridiagonalization of the Hamiltonian for the construction of the correction vector $|\text{c.v.}\rangle = \frac{1}{\omega - H + i\eta}\hat{O}|\text{g.s.}\rangle$, where $\hat{O}$ is the relevant operator. In the current work, we have imposed a maximum Lanczos error of $10^{-8}$ allowing at most 200 iterations (as opposed to standard $10^{-12}$ Lanczos precision of ground state computations) to avoid the proliferation of a larger number of Lanczos steps at high excitation energies and the consequent need for CPU consuming reorthogonalization of the Lanczos vectors.

## Data availability

The data that support the findings of this study are available from the corresponding authors on reasonable request.

## Code availability

The DQMC code can be downloaded at https://github.com/sli43/DQMC-for-the-1D-corner-shared-cuprates. The DMRG code can be downloaded at https://github.com/g1257/dmrgpp/.

Received: 21 April 2021; Accepted: 6 September 2021;
Published online: 23 September 2021

## References

1. Keimer, B., Kivelson, S. A., Norman, M. R., Uchida, S. & Zaanen, J. From quantum matter to high-temperature superconductivity in copper oxides. *Nature* **518**, 179–186 (2015).
2. LeBlanc, J. P. F. et al. Solutions of the two-dimensional Hubbard model: benchmarks and results from a wide range of numerical algorithms. *Phys. Rev. X* **5**, 041041 (2015).
3. Jiang, H.-C. & Devereaux, T. P. Superconductivity in the doped Hubbard model and its interplay with next-nearest hopping $t'$. *Science* **365**, 1424–1428 (2019).
4. Qin, M. et al. Absence of superconductivity in the pure two-dimensional Hubbard model. *Phys. Rev. X* **10**, 031016 (2020).
5. Maier, T. A., Jarrell, M., Schulthess, T. C., Kent, P. R. C. & White, J. B. Systematic study of *d*-wave superconductivity in the 2D repulsive Hubbard model. *Phys. Rev. Lett.* **95**, 237001 (2005).
6. Gull, E., Parcollet, O. & Millis, A. J. Superconductivity and the pseudogap in the two-dimensional Hubbard model. *Phys. Rev. Lett.* **110**, 216405 (2013).
7. Jiang, Y.-F., Zaanen, J., Devereaux, T. P. & Jiang, H.-C. Ground state phase diagram of the doped Hubbard model on the four-leg cylinder. *Phys. Rev. Res.* **2**, 033073 (2020).
8. Mousatov, C. H., Esterlis, I. & Hartnoll, S. A. Bad metallic transport in a modified Hubbard model. *Phys. Rev. Lett.* **122**, 186601 (2019).
9. Huang, E. W., Sheppard, R., Moritz, B. & Devereaux, T. P. Strange metallicity in the doped Hubbard model. *Science* **366**, 987–990 (2019).
10. Šimkovic, F. et al. Extended crossover from a Fermi liquid to a quasiantiferromagnet in the half-filled 2D Hubbard model. *Phys. Rev. Lett.* **124**, 017003 (2020).
11. Chen, X., LeBlanc, J. P. F. & Gull, E. Simulation of the NMR response in the pseudogap regime of the cuprates. *Nat. Commun.* **8**, 14986 (2017).
12. Robinson, N. J., Johnson, P. D., Rice, T. M. & Tsvelik, A. M. Anomalies in the pseudogap phase of the cuprates: competing ground states and the role of Umklapp scattering. *Rep. Prog. Phys.* **82**, 126501 (2019).
13. Wu, W. et al. Pseudogap and Fermi-surface topology in the two-dimensional Hubbard model. *Phys. Rev. X* **8**, 021048 (2018).
14. Zheng, B.-X. et al. Stripe order in the underdoped region of the two-dimensional Hubbard model. *Science* **358**, 1155–1160 (2017).
15. Ehlers, G., White, S. R. & Noack, R. M. Hybrid-space density matrix renormalization group study of the doped two-dimensional Hubbard model. *Phys. Rev. B* **95**, 125125 (2017).
16. Darmawan, A. S., Nomura, Y., Yamaji, Y. & Imada, M. Stripe and superconducting order competing in the Hubbard model on a square lattice studied by a combined variational Monte Carlo and tensor network method. *Phys. Rev. B* **98**, 205132 (2018).
17. Huang, E. W., Mendl, C. B., Jiang, H.-C., Moritz, B. & Devereaux, T. P. Stripe order from the perspective of the Hubbard model. *npj Quantum Mater.* **3**, 22 (2018).
18. Jia, C. J. et al. Persistent spin excitations in doped antiferromagnets revealed by resonant inelastic light scattering. *Nat. Commun.* **5**, 3314 (2014).
19. Ishii, K. et al. High-energy spin and charge excitations in electron-doped copper oxide superconductors. *Nat. Commun.* **5**, 3714 (2014).
20. LeBlanc, J. P. F. et al. Magnetic susceptibility and simulated neutron signal in the two-dimensional Hubbard model. *Phys. Rev. B* **100**, 075123 (2019).
21. Rybicki, D., Jurkutat, M., Reichardt, S., Kapusta, C. & Haase, J. Perspective on the phase diagram of cuprate high-temperature superconductors. *Nat. Commun.* **7**, 11413 (2016).
22. Achkar, A. J. et al. Orbital symmetry of charge-density-wave order in $La_{1.875}Ba_{0.125}CuO_4$ and $YBa_2Cu_3O_{6.67}$. *Nat. Mater.* **15**, 616–620 (2016).

23. Jurkutat, M. et al. Distribution of electrons and holes in cuprate superconductors as determined from $^{17}O$ and $^{63}Cu$ nuclear magnetic resonance. *Phys. Rev. B* **90**, 140504 (2014).
24. Rubtsov, A. N., Katsnelson, M. I., Lichtenstein, A. I. & Georges, A. Dual fermion approach to the two-dimensional Hubbard model: antiferromagnetic fluctuations and Fermi arcs. *Phys. Rev. B* **79**, 045133 (2009).
25. Sun, P. & Kotliar, G. Extended dynamical mean-field theory and GW method. *Phys. Rev. B* **66**, 085120 (2002).
26. Toschi, A., Katanin, A. A. & Held, K. Dynamical vertex approximation: a step beyond dynamical mean-field theory. *Phys. Rev. B* **75**, 045118 (2007).
27. Katanin, A. A., Toschi, A. & Held, K. Comparing pertinent effects of antiferromagnetic fluctuations in the two- and three-dimensional Hubbard model. *Phys. Rev. B* **80**, 075104 (2009).
28. White, S. R. et al. Numerical study of the two-dimensional Hubbard model. *Phys. Rev. B* **40**, 506–516 (1989).
29. Huang, E. W. et al. Numerical evidence of fluctuating stripes in the normal state of high-$T_c$ cuprate superconductors. *Science* **358**, 1161–1164 (2017).
30. Orús, R. A practical introduction to tensor networks: matrix product states and projected entangled pair states. *Ann. Phys.* **349**, 117–158 (2014).
31. Orús, R. Tensor networks for complex quantum systems. *Nat. Rev. Phys.* **1**, 538–550 (2019).
32. Qin, M., Shi, H. & Zhang, S. Benchmark study of the two-dimensional Hubbard model with auxiliary-field quantum Monte Carlo method. *Phys. Rev. B* **94**, 085103 (2016).
33. Frick, M., Pattnaik, P. C., Morgenstern, I., Newns, D. M. & von der Linden, W. Monte Carlo study of superconductivity in the three-band Emery model. *Phys. Rev. B* **42**, 2665–2668 (1990).
34. Avella, A., Mancini, F., Mancini, F. P. & Plekhanov, E. Emery vs. Hubbard model for cuprate superconductors: a composite operator method study. *Eur. Phys. J. B* **86**, 265 (2013).
35. Mai, P., Balduzzi, G., Johnston, S. & Maier, T. A. Orbital structure of the effective pairing interaction in the high-temperature superconducting cuprates. *npj Quantum Mater.* **6**, 26 (2021).
36. Liu, K., Lu, Z.-Y. & Xiang, T. Electronic structures of quasi-one-dimensional cuprate superconductors $Ba_2CuO_{3+\delta}$. *Phys. Rev. Mater.* **3**, 044802 (2019).
37. Chen, Z. et al. Anomalously strong near-neighbor attraction in doped 1D cuprate chains. Science **373**, 1235–1239 (2021).
38. Li, S., Tang, Y., Maier, T. A. & Johnston, S. Phase competition in a one-dimensional three-orbital Hubbard−Holstein model. *Phys. Rev. B* **97**, 195116 (2018).
39. Kühner, T. D. & White, S. R. Dynamical correlation functions using the density matrix renormalization group. *Phys. Rev. B* **60**, 335–343 (1999).
40. Nocera, A. & Alvarez, G. Spectral functions with the density matrix renormalization group: Krylov-space approach for correction vectors. *Phys. Rev. E* **94**, 053308 (2016).
41. Ami, T. et al. Magnetic susceptibility and low-temperature structure of the linear chain cuprate $Sr_2CuO_3$. *Phys. Rev. B* **51**, 5994–6001 (1995).
42. Kojima, K. M. et al. Reduction of ordered moment and Néel temperature of quasi-one-dimensional antiferromagnets $Sr_2CuO_3$ and $Ca_2CuO_3$. *Phys. Rev. Lett.* **78**, 1787–1790 (1997).
43. Walters, A. C. et al. Effect of covalent bonding on magnetism and the missing neutron intensity in copper oxide compounds. *Nat. Phys.* **5**, 867–872 (2009).
44. Zaliznyak, I. A. et al. Spinons in the strongly correlated copper oxide chains in $SrCuO_2$. *Phys. Rev. Lett.* **93**, 087202 (2004).
45. Schlappa, J. et al. Spin-orbital separation in the quasi-one-dimensional Mott insulator $Sr_2CuO_3$. *Nature* **485**, 82–85 (2012).
46. Schlappa, J. et al. Probing multi-spinon excitations outside of the two-spinon continuum in the antiferromagnetic spin chain cuprate $Sr_2CuO_3$. *Nat. Commun.* **9**, 5394 (2018).
47. Kumar, U., Nocera, A., Dagotto, E. & Johnston, S. Multi-spinon and antiholon excitations probed by resonant inelastic x-ray scattering on doped one-dimensional antiferromagnets. *New J. Phys.* **20**, 073019 (2018).
48. Neudert, R. et al. Manifestation of spin-charge separation in the dynamic dielectric response of one-dimensional $Sr_2CuO_3$. *Phys. Rev. Lett.* **81**, 657–660 (1998).
49. Penc, K. & Stephan, W. Dynamical correlations in one-dimensional charge-transfer insulators. *Phys. Rev. B* **62**, 12707–12714 (2000).
50. Maiti, K. & Sarma, D. D. Spectroscopic investigation of the electronic structure of the hole-doped one-dimensional cuprates $Ca_2CuO_3$ and $Sr_2CuO_3$. *Phys. Rev. B* **65**, 174517 (2002).
51. Simutis, G. et al. Spin pseudogap in Ni-doped $SrCuO_2$. *Phys. Rev. Lett.* **111**, 067204 (2013).
52. Karmakar, K., Bag, R., Skoulatos, M., Rüegg, C. & Singh, S. Impurities in the weakly coupled quantum spin chains $Sr_2CuO_3$ and $SrCuO_2$. *Phys. Rev. B* **95**, 235154 (2017).
53. Neudert, R. et al. Four-band extended Hubbard hamiltonian for the one-dimensional cuprate $Sr_2CuO_3$: distribution of oxygen holes and its relation to strong intersite coulomb interaction. *Phys. Rev. B* **62**, 10752–10765 (2000).
54. Wohlfeld, K., Nishimoto, S., Haverkort, M. W. & van den Brink, J. Microscopic origin of spin-orbital separation in $Sr_2CuO_3$. *Phys. Rev. B* **88**, 195138 (2013).
55. Nocera, A. et al. Computing resonant inelastic x-ray scattering spectra using the density matrix renormalization group method. *Sci. Rep.* **8**, 11080 (2018).
56. Zhang, F. C. & Rice, T. M. Effective hamiltonian for the superconducting Cu oxides. *Phys. Rev. B* **37**, 3759–3761 (1988).
57. Tjeng, L. H. et al. Spin-resolved photoemission on anti-ferromagnets: direct observation of Zhang-Rice singlets in CuO. *Phys. Rev. Lett.* **78**, 1126–1129 (1997).
58. Kim, B. J. et al. Distinct spinon and holon dispersions in photoemission spectral functions from one-dimensional $SrCuO_2$. *Nat. Phys.* **2**, 397–401 (2006).
59. Nocera, A., Essler, F. H. L. & Feiguin, A. E. Finite-temperature dynamics of the Mott insulating Hubbard chain. *Phys. Rev. B* **97**, 045146 (2018).
60. Nocera, A., Patel, N. D., Fernandez-Baca, J., Dagotto, E. & Alvarez, G. Magnetic excitation spectra of strongly correlated quasi-one-dimensional systems: Heisenberg versus Hubbard-like behavior. *Phys. Rev. B* **94**, 205145 (2016).
61. Pärschke, E. M. et al. Numerical investigation of spin excitations in a doped spin chain. *Phys. Rev. B* **99**, 205102 (2019).
62. Kumar, U. et al. Spectroscopic signatures of next-nearest-neighbor hopping in the charge and spin dynamics of doped one-dimensional antiferromagnets. *Phys. Rev. B* **102**, 075134 (2020).
63. Lorenzana, J., Seibold, G. & Coldea, R. Sum rules and missing spectral weight in magnetic neutron scattering in the cuprates. *Phys. Rev. B* **72**, 224511 (2005).
64. Lee, W. S. et al. Asymmetry of collective excitations in electron- and hole-doped cuprate superconductors. *Nat. Phys.* **10**, 883–889 (2014).
65. Lin, J. et al. Doping evolution of the charge excitations and electron correlations in electron-doped superconducting $La_{2-x}Ce_xCuO_4$. *npj Quantum Mater.* **5**, 4 (2020).
66. Li, S. *Numerical Study of the Electron-Phonon Interaction in Multiorbital Materials*. Ph.D. thesis, University of Tennessee (2018).
67. Fuchs, S., Pruschke, T. & Jarrell, M. Analytic continuation of quantum Monte Carlo data by stochastic analytical inference. *Phys. Rev. E* **81**, 056701 (2010).
68. Loh, E. Y. et al. Sign problem in the numerical simulation of many-electron systems. *Phys. Rev. B* **41**, 9301–9307 (1990).
69. White, S. R. Density matrix formulation for quantum renormalization groups. *Phys. Rev. Lett.* **69**, 2863–2866 (1992).
70. White, S. R. Density-matrix algorithms for quantum renormalization groups. *Phys. Rev. B* **48**, 10345–10356 (1993).
71. Alvarez, G. The density matrix renormalization group for strongly correlated electron systems: a generic implementation. *Comput. Phys. Commun.* **180**, 1572–1578 (2009).
72. Nocera, A. et al. Doping evolution of charge and spin excitations in two-leg Hubbard ladders: Comparing DMRG and FLEX results. *Phys. Rev. B* **97**, 195156 (2018).


## Acknowledgements

We thank C.D. Batista and T.A. Maier for valuable discussions and comments on the manuscript. This work was supported by the U.S. Department of Energy, Office of Basic Energy Sciences, Materials Sciences, and Engineering Division. S.J. acknowledges support from the Scientific Discovery through Advanced Computing (SciDAC) program funded by the U.S. Department of Energy, Office of Science, Advanced Scientific Computing Research and Basic Energy Sciences, Division of Materials Sciences and Engineering. A.N. acknowledges support from the Max Planck-UBC-UTokyo Center for Quantum Materials and Canada First Research Excellence Fund (CFREF) Quantum Materials and Future Technologies Program of the Stewart Blusson Quantum Matter Institute (SBQMI), and the Natural Sciences and Engineering Research Council of Canada (NSERC). U.K. acknowledges support from the US DOE NNSA under Contract No. 89233218CNA000001 through the LDRD Program. This research used resources of the Compute and Data Environment for Science (CADES) at the Oak Ridge National Laboratory, which is supported by the Office of Science of the U.S. Department of Energy under Contract No. DE-AC05-00OR22725. This work also used computational resources and services provided by Compute Canada and Advanced Research Computing at the University of British Columbia.

## Author contributions

S.L. performed DQMC calculations. A.N. performed DMRG calculations. S.L. and U.K. performed exact diagonalization calculations. S.L. and S.J. developed the DQMC code. S.J. supervised the project. All authors contributed to analyzing the data and writing the paper.

## Competing interests

The authors declare no competing interests.

## Additional information

**Supplementary information** The online version contains supplementary material available at https://doi.org/10.1038/s42005-021-00718-w.

**Correspondence** and requests for materials should be addressed to Shaozhi Li or Steven Johnston.

**Peer review information** *Communications Physics* thanks the anonymous reviewers for their contribution to the peer review of this work. Peer reviewer reports are available.

**Reprints and permission information** is available at http://www.nature.com/reprints

**Publisher's note** Springer Nature remains neutral with regard to jurisdictional claims in published maps and institutional affiliations.